

SCIENTIFIC REPORTS



Low-temperature electrodeposition approach leading to robust mesoscopic anatase TiO₂ films

Snehangshu Patra^{1,2}, Christian Andriamiadamanana^{1,2}, Michal Tulodziecki¹, Carine Davoisne^{1,2}, Pierre-Louis Taberna^{2,3} & Frédéric Sauvage^{1,2}

Received: 13 October 2015

Accepted: 25 January 2016

Published: 25 February 2016

Anatase TiO₂, a wide bandgap semiconductor, likely the most worldwide studied inorganic material for many practical applications, offers unequal characteristics for applications in photocatalysis and sun energy conversion. However, the lack of controllable, cost-effective methods for scalable fabrication of homogeneous thin films of anatase TiO₂ at low temperatures (ie. < 100 °C) renders up-to-date deposition processes unsuited to flexible plastic supports or to smart textile fibres, thus limiting these wearable and easy-to-integrate emerging technologies. Here, we present a very versatile template-free method for producing robust mesoporous films of nanocrystalline anatase TiO₂ at temperatures of/or below 80 °C. The individual assembly of the mesoscopic particles forming ever-demonstrated high optical quality beads of TiO₂ affords, with this simple methodology, efficient light capture and confinement into the photo-anode, which in flexible dye-sensitized solar cell technology translates into a remarkable power conversion efficiency of 7.2% under A.M.1.5G conditions.

The seminal work of Honda *et al.*¹ back to 1972 demonstrated the feasibility to split water molecules by exposing TiO₂ surface to incident sunlight. This finding has opened up new avenues for integrating this class of material into photonic displays. The significant attentiveness to this material also stems from its 3d⁰ electronic configuration, particularly sensitive to the introduction of punctual defects by doping or by reductive post-thermal treatment. This offers a very unique and easy way for bandgap engineering, providing in theory a solution to its intrinsic drawback of low solar spectrum absorption resulting from its wide indirect bandgap of 3.2 eV². Consequently, this latter can be tuned to a remarkable range either to a narrowed black 1.85 eV bandgap or inversely blue-shifted to 3.8 eV owing to quantum confinement effect taking place below a size threshold of ca. 2 nm³⁻⁵. Since its first integration into dye-sensitized solar cells technology by O'Regan *et al.* in 1991⁶⁻⁸, even though different mesostructures have been tailored⁹ and alternate materials scrutinized to date¹⁰, nanocrystals of anatase TiO₂ still remain the leading contender affording the highest power conversion efficiency and stability in conjunction with either heteroleptic ruthenium polypyridil complexes or as a scaffold in hybrid organic-inorganic perovskite absorbers¹¹⁻¹³.

In a typical synthetic procedure, the anatase requires a temperature of a few hundred of degrees in solid-state reactions to get crystallized¹⁴. This temperature can be lowered by combining temperature with pressure using conventional hydro(solvo)thermal approaches^{15,16} or by more controlled sol-gel/thermolysis methods at mild to even room-temperature^{17,18}. This heating requirement is also true when using electrochemical, vapor or vacuum deposition techniques for preparing functional thin films. It typically undergoes first a deposition of titanium-based clusters, followed by a thermal post-annealing process to crystallize the film^{19,20}. Consequently, this second step restricts the utilization of a broad range of substrates among the flexible plastics (PEN, PET...) ²¹ or natural/synthetics fibres for the smart textiles in which TiO₂ as a functional material plays a pivotal role. Investigation on TiO₂ electrodeposition has remained scarce so far owing to the difficulties to manipulate Ti³⁺ in aqueous solution requiring at once highly acidic chemical bath and argon conditions to maintain Ti³⁺ stable against hydrolysis (pH > 2) and oxidation to air²². This was partially overcome recently by the use of ionic liquid-based chemical bath including TiCl₄ as a precursor, even though still requiring the step of post-annealing for getting crystalline films²³. With the aim to circumvent this critical last step, we recently discussed a mechanism

¹Laboratoire de Réactivité et Chimie des Solides, Université de Picardie Jules Verne, CNRS UMR 7314, 33, rue Saint Leu, 80039 Amiens, France. ²Réseau sur le Stockage Electrochimique de l'Energie (RS2E), FR CNRS 3459, France.

³Université Paul Sabatier, Toulouse III, CIRIMAT, CNRS UMR 5085, 118, Route de Narbonne, 31062 Toulouse cedex 09, France. Correspondence and requests for materials should be addressed to F.S. (email: frederic.sauvage@u-picardie.fr)

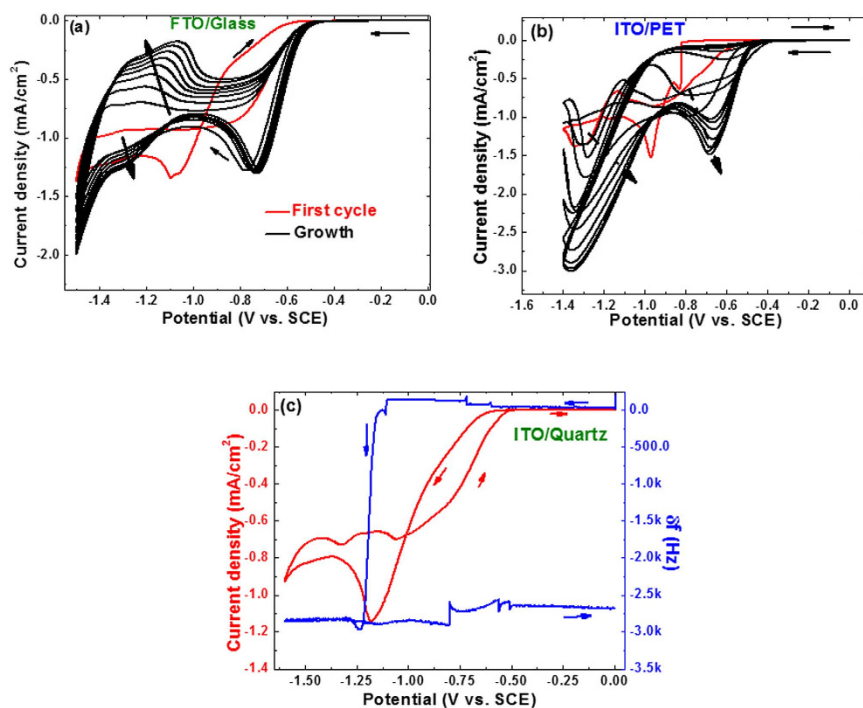
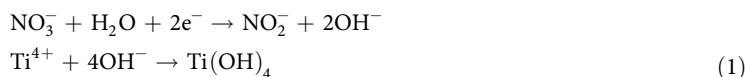


Figure 1. Cyclic voltamperometry experiments on (a) FTO/Glass, (b) ITO/PET electrode over 10 cycles in a chemical bath of pH = 1.8 consisting of 0.01 mol/L of TiCl_4 and 0.2 mol/L of KNO_3 at a sweep rate of 10 mV/s (c) ITO coated Electrochemical Quartz Cristal Microbalance (EQCM) measurement of the first cycle.

of dehydration of $\text{Ti}(\text{OH})_4$ particles taking place at room-temperature which leads to well-crystallized nanoparticles of anatase TiO_2 ^{24,25}. Taking advantage of these preceding works, we herein report a very soft electrodeposition procedure, versatile to all kind of conductive substrates, and easy to handle and to scale-up on larger surfaces, which offers highly porous and robust crystalline mesoscopic films of anatase TiO_2 not only on FTO-conductive glass but also on flexible plastic PEN-ITO (PolyEthylene Naphtalate). Based on optimized electrodeposition conditions, we demonstrate a flexible dye-sensitized solar cells affording a power conversion efficiency of 7.2% under A.M.1.5G conditions when associated to the robust heteroleptic C106 ruthenium dye.

Results

Figure 1 gathers the successive cyclic voltammograms (CV) recorded between 0 to -1.5 V vs. SCE at $\nu = 10$ mV/s upon a conductive FTO-glass electrode. The aqueous chemical bath is composed of 0.2 mol/L of KNO_3 and 0.01 mol/L of TiCl_4 . The strategy employed consists on nitrate reduction approach largely scrutinized for ZnO electrodeposition to provide excellent control on the deposit's texture²⁶. Transposed in this work for first time to titanium chemistry, the electrochemical reduction of nitrates NO_3^- to nitrites NO_2^- releases at the electrode's surface two equivalents of hydroxide responsible for a noticeable local pH increases²⁶. In this case, this local pH increases at the electrode/solution interface triggers the precipitation of titanium hydroxide when this latter becomes greater than 3 accordingly to the equations below²⁷:



The nitrate reduction is a slow two-electron redox process involving nitrogen-oxygen bond cleavage followed by a structural rearrangement^{28,29}. This simple approach circumvents the use of both highly acidic and reductive conditions required when using the air-sensitive TiCl_3 or the pyrophoric derivatives.

Employing the aforementioned chemical bath composition, onset of a cathodic current starts at *ca.* -0.60 V (vs. SCE) on FTO glass electrode or on ITO/PET (Fig. 1). On the first cycle, the cathodic peak shows two components in the current raising, a first attributed to dissolved oxygen reduction followed by nitrate reduction³⁰. The maximum peak current reaches a density of *ca.* 1.3 mA/cm² at -1.1 V (vs. SCE). At greater overpotentials, a steady-state regime is systematically noticed before the occurrence of the expected cathodic branch starting at -1.45 V (vs. SCE) corresponding to hydrogen evolution. This intermediate steady-state plateau corresponds to the nitrate mass transport control for which a diffusion coefficient in the range of 10^{-5} cm²/s has been reported in the literature^{30–32}. One can also notice that the first cycle of the CV features a reduction/oxidation loop which tends to suggest an effective change of the electrode surface. Note that no titanium metal deposit is formed at this range of potentials which could have explained such loop owing to a metal deposition/dissolution process. The first and subsequent cycles are systematically different regardless of the type of electrodes. This is different not only in shape but also in terms of overpotential, corroborating with the modification of electrode surface during

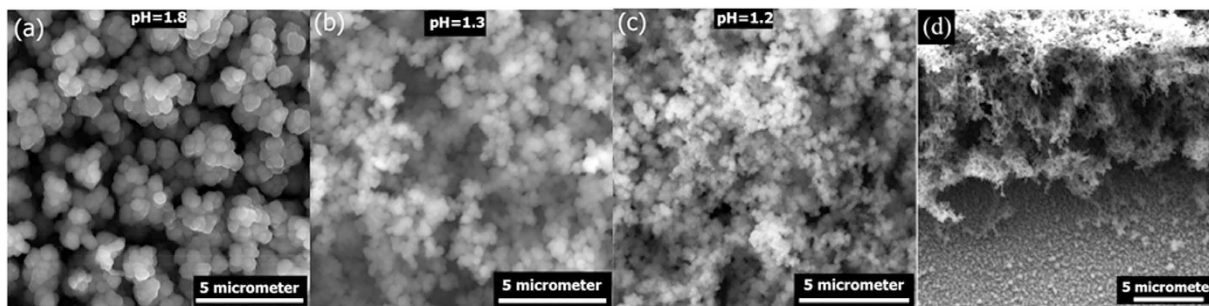


Figure 2. Comparison of SEM micrographs. This compares $\text{Ti}(\text{OH})_4$ electrodeposited on ITO/PET electrode at a sweep rate of 10 mV/s in the potential window of -0.9 V to 0 V for 40 cycles. The chemical bath is composed of 0.01 mol/L of $\text{TiCl}_4(\text{aq})$ and 0.2 mol/L of KNO_3 . The pH of the chemical bath was adjusted by adding $\text{HCl}(\text{aq})$ to (a) 1.7, (b) 1.3, (c) 1.2. (d) is a cross section SEM micrograph of the as-deposited $\text{Ti}(\text{OH})_4$ film at pH = 1.2.

the first cycle. The second and ensuing cycles are characterized by a positive shift of the cathodic peak by around 300 mV and a better defined single faradaic phenomenon (Fig. 1a,b). This reveals that when modified, the new surface exhibits greater electrocatalytic activities with respect to nitrate and water reductions. However, the value of steady state current from nitrates mass transport control becomes reduced, thus indicating a lowering in its diffusion flux in the vicinity of the new electrode's surface. Compared to FTO, ITO/PET electrode shows exactly same trend. On this electrode, the two steps in reduction are better defined with a cathodic peak at -0.83 V corresponding to dissolved oxygen reduction and -0.97 V (vs. SCE) for nitrate reduction (Fig. 1b). A similar shift of +300 mV after the first cycle is also experienced.

To better insight on the redox mechanism during this first cycle, we used electrochemical ITO coated quartz crystal microbalance (EQCM) to monitor the evolution of crystal resonance frequency, therefore the mass by considering Sauerbrey's equation³³, as a function of the applied potential at the electrode (Fig. 1c). The first cycle recorded on EQCM reproduces exactly the voltamperogram on FTO, at the exception of a slightly greater overpotential when using the quartz crystal as an electrode. The first shoulder aforementioned, taking place here at ca. -0.8 V (vs. SCE), does not affect the quartz resonance frequency. This means that such reduction process is not initiating any deposit upon the electrode which again gives credit to its attribution to oxygen reduction. This falls in contrast to the following faradaic phenomenon which induces a drastic change on the crystal resonance frequency from ca. 0 to -3 kHz. This leads to the formation of a clear whitish deposit on the electrode. This film, amorphous by x-ray diffraction, corresponds to $\text{Ti}(\text{OH})_4$ whose formation is triggered by the local increase in pH contributing to shift the stabilized solvated Ti^{4+} cations towards their hydrolyzed form $\text{Ti}(\text{OH})_4$ beyond $\text{pH} = 2^{34}$.

One advantage of electrodeposition technique over vacuum counterparts is the number of freedom parameters which can offer a very precise control on structural polymorphism, morphology, thickness or porosity of the deposit. In this work, we specifically control the ratio of the concentration of the species involved in electrodeposition, pH of the chemical bath along with cathodic-anodic scan range, various deposition methodologies (galvanostatic, potentiostatic and potentiodynamic) and substrate for obtaining highly porous and well-covering robust deposit.

A first parameter concerns the molar ratio between TiCl_4 and KNO_3 , adjusted by increasing NO_3^- while keeping Ti^{4+} constant. This ratio controls the proportion between hydroxide produced at electrode surface and the concentration of Ti^{4+} at its surface. Ratios between 1:6 and 1:50 ($\text{Ti}^{4+}:\text{NO}_3^-$) were investigated. Well covering and robust deposits are not achieved at molar ratio lower than 1:14 and greater than 1:20. The film thickness for the same amount of cycles is increasing with the amount of KNO_3 as one could expect, eg. $5 \mu\text{m}$ for 1:6 ratio to $30 \mu\text{m}$ for 1:20. Keeping an optimized ratio of 1:20, the second parameter, pH of the chemical bath was varied. We found this factor extremely crucial. It is not only changing the film morphology but it also prevents the formation of cracks. A well-controlled pH affords robust, homogeneous and well-covering film. This is illustrated in the Fig. 2 in which we gathered a representative series of SEM micrographs depicting how the film morphology evolves after 40 cycles at different pH from 1.7 to 1.2. Decreasing the pH, although to such a low extent, considerably affects the particle size without modifying the particle morphology. For pH = 1.7, the film is formed of agglomerated well monodisperse spherical particles somehow resembling to small cauliflowers for which the size of the particles is in the range of ~ 500 nm.

This particle size decreases to ca. 300 nm towards pH = 1.2. This underlines the noticeable influence of the pH on the kinetic competition between nucleation and growth; nucleation being promoted towards more acidic conditions. The cross-section view of this latter film shows a thickness of $15 \mu\text{m}$ consisting of well-interconnected particles with high porosity all throughout the depth of the film (Fig. 2d). At pH greater than 2, a white precipitate is progressively forming into the chemical bath owing to hydrolysis of Ti^{4+} . In opposite, films electrodeposited at pH below 1.2 becomes fragile and crumbly owing to an excessive porosity, likely generated by the promoted hydrogen evolution on the surface of the electrode³⁵. This very close relationship between film's morphology and chemical bath pH also gets retranscribed in the cyclic voltamperograms where more current is systematically observed when the pH is acidified (Fig. S1a). The film thickness increases substantially with the pH from 12.5 to 21 and $25.5 \mu\text{m}$ thick electrode at pH = 1.2, 1.3 and 1.7, respectively (Fig. S1b). This evolution comes in opposite trend to the evolution of charge density obtained by integration of the voltamperograms over the 40 cycles. This is explained by the competition between nitrate reduction and hydrogen evolution, the latter becoming

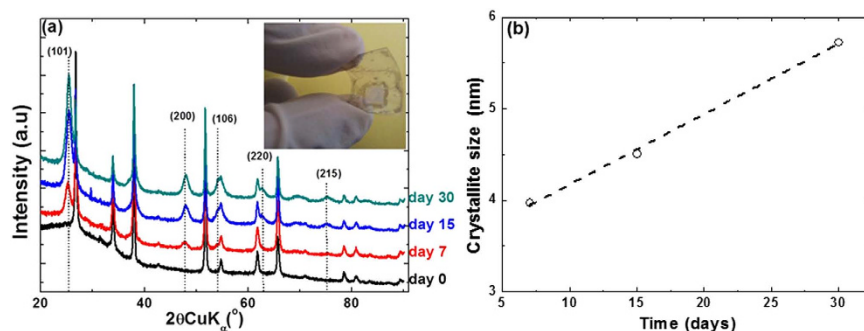


Figure 3. Evolution of the XRD diffractograms (a) and crystallite size (b) upon ageing of optimized as-deposited films at 80 °C in 0.1 mol/L $\text{NH}_4\text{F}_{(\text{aq})}$ solution (substrate FTO glass).

predominant when moving to low pH. This can be seen also on the electrode surface with the development of hydrogen bubbles forming close to the cathodic to anodic vertex potential. Such a heterogeneous competition between hydrogen formation and nitrate reduction is particularly fascinating as it provides a very new way, without any means of template, to control dense-to-porous and meso-to-macroporosity depending on the potentiostatic conditions, as carefully demonstrated previously on ZnO^{35} .

Although the cyclic voltamperometry method is often never considered for electrodeposition since neither the redox process involved is selective owing to potential variations during electrodeposition (by contrast to the potentiostatic method) nor giving a control of the mass transport as for galvanostatic techniques, in this particular case the cyclic voltamperometry revealed to be very suitable to reach covering films with excellent adhesion properties. This is in good agreement with previous experiences by An *et al.*³⁶ The value of cathodic to anodic reverse potential is crucial for the deposition quality because of the hydrogen production. This potential is optimum at -1.5 V (vs. SCE) for FTO and -0.9 V (vs. SCE) for ITO/PET in the optimized formulation of the chemical bath. At greater potentials, the deposition yields to dense and poor covering films whereas at excessive low vertex potentials the excessive hydrogen production hampers good film adhesion upon the electrode. The optimized bath composition is perfectly stable for temperatures below 40 °C. Beyond, the titanium tetrachloride is getting gradually hydrolysed. Regardless of the deposition conditions, the as-deposited films were systematically amorphous by x-ray diffraction, as for the other electrodeposition methodology proposed so far. This is not surprising since we recently demonstrated that despite using highly stable ionic liquid chemical bath for which depositions performed up to 150 °C were still insufficient to overcome the energy barrier for electrocrystallization²³. In this work, we are bypassing this important drawback by means of a simple and versatile method to convert the initial amorphous films to well-crystallized anatase structure by ageing the film into an aqueous solution containing 0.1 mol/L of $\text{NH}_4\text{F}_{(\text{aq})}$. This is shown in Fig. 3a in which we collect a series of XRD diffractograms recorded until 30 days of ageing at 80 °C. A gradual crystallization of the anatase polymorph is experienced with a predominance of the most stable and most electro-active (101) diffraction plane³⁷. The role of NH_4F is at once to assist the solid-state dehydration process of the film to onset its crystallization²⁴ and at same time to prevent the formation of brookite as part as anatase thanks to fluoride anion capping at the particle surface^{24,38–42}. This solid-state dehydration process, inducing particles crystallization, was further probed by EQCM experiments (Fig. S2). The δf of freshly prepared $\text{Ti}(\text{OH})_4/\text{ITO}$ -Quartz was collected in air for 10 minutes until a stable response δf of $-12,000$ Hz was obtained. Once aged at 80 °C in 0.1 mol/L $\text{NH}_4\text{F}_{(\text{aq})}$, the frequency started to increase substantially from $-12,000$ Hz to $-2,535$ Hz for 2 hours ageing time and to $-1,242$ Hz after 7 hours. The increase in δf , i.e. decrease in mass loss (%) by considering Sauerbrey's equation³³, is reported as a function of ageing time in Fig. S2b. This evolution describes a single exponential, reaching a plateau after 4 hours of ageing at 80 °C and beyond 7 hours at room-temperature. This suggests that the crystallization process is a two steps process not concomitant with dehydration and that the rate limiting step for crystallization is not dehydration but the subsequent structural rearrangement yielding to the anatase crystal structure.

This means that this method previously developed for anodized titanium foils^{42,43} and for powders^{18,24} can be perfectly extended to electrodeposited films. All along the duration of ageing, broad diffraction peaks are observed referring to the nano-size nature of the crystallites (Fig. 3). During ageing, the crystallite size increases linearly from 4 to a maximum of 6 nm as described in Fig. 3b. Longer time does not increase further the crystallite size, signifying 30 days is needed to completely convert the pristine amorphous particles to anatase.

The particle morphology does not evolve drastically during this crystallization process by contrast to previous reports on powders showing a solid-state reorganisation of the nanoparticles (Fig. 4)^{24,44}. In good consistency with XRD, the electron diffraction pattern evolves from diffuse rings, confirming the amorphous character of the as-deposited particles, to well-defined rings ascribed accordingly to the anatase. After ageing, the film is composed of well-crystallized monolithic particles exhibiting rectangular shape of size between 5 to 10 nm. These particles predominantly consist of (101) planes of anatase TiO_2 (0.323 nm lattice spacing) (Fig. 4c inset). This suggests that the spherical particles of 300 nm size observed by SEM are composed of these aggregated primary particles forming beads. The optical bandgap of the films have been evaluated by UV-visible spectroscopy in diffuse reflectance mode using Kubelka-Munk approach (Fig. S3). The crystallization process reduces the optical bandgap from 3.44 eV of amorphous $\text{Ti}(\text{OH})_4$ ⁴⁵ to 3.14 eV in good agreement with the values reported in the literature for anatase^{46–48}.

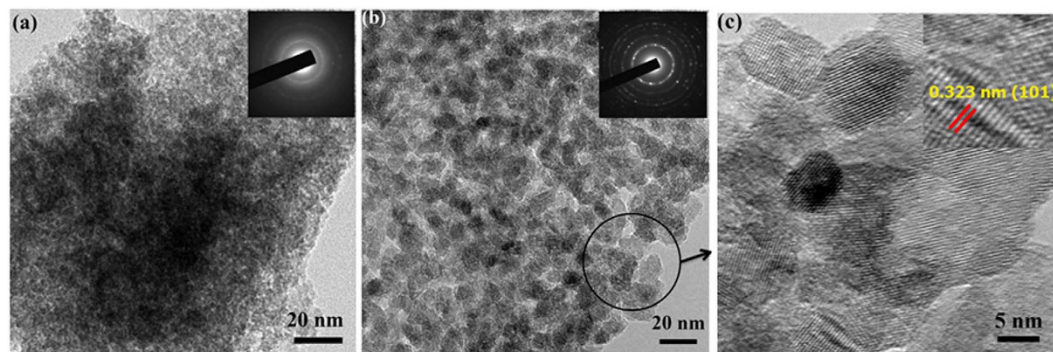


Figure 4. Comparison of TEM micrographs and SAED patterns for (a) as-prepared amorphous $\text{Ti}(\text{OH})_4$ and (b) TiO_2 obtained after 15 days ageing in $\text{NH}_4\text{F}_{(\text{aq})}$ (c) HRTEM image of TiO_2 showing dominance of (101) diffraction planes.

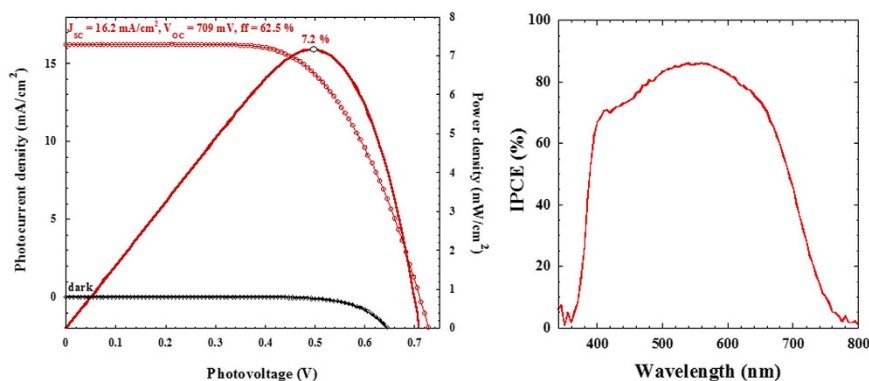


Figure 5. (J–V) curve under dark condition and under A.M. 1.5G illumination of flexible dye-sensitized solar cells composed of electrodeposited TiO_2 electrode of ca. $12\ \mu\text{m}$ thick sensitized with C106 dye. The related IPCE action spectra is reported.

This two-step method to reach low-temperature crystalline films of mesoscopic anatase TiO_2 is versatile to all conducting substrates. Taking advantage on the realization of such beads of TiO_2 for which this kind of morphology has demonstrated outstanding light-to-electricity conversion efficiency and improved charge collection efficiency in dye-sensitized solar cells owing their bi-functionality combining high surface area for high dye-loading and light confinement improvement in the photo-anode accordingly to Mie scattering theory^{49–52}, the performances demonstrated on flexible dye-sensitized solar cells in conjunction with the ruthenium polypyridyl C106 complex⁵³ are among the best values reported so far in the literature on flexible devices^{54–57} by attaining a power conversion efficiency of 7.2% under standard A.M.1.5G conditions ($100\ \text{mW}/\text{cm}^2$) (Fig. 5). The related IPCE action spectra shows a maximum of quantum efficiency of 85% at 556 nm before to decline towards 750 nm. Its integration leads to a value of $15.9\ \text{mA}/\text{cm}^2$, that is excellent agreement with the short-circuit current density measured with 3A class sun simulator. For comparison using same thickness, dye and electrolyte composition, P25-based glass FTO device was achieving 7.1% and 9.3% on 20 nm-based nanocrystalline TiO_2 without scattering layer (Fig. S4).

Conclusions

We describe a facile and a versatile two-step methodology using the electrodeposition technique to obtain porous and mesoscopic film of anatase TiO_2 upon flexible PET/ITO substrate. This method, employing a safer chemical bath, bypasses the current technological obstacle of post-annealing to crystallize the anatase structure. Consequently, this approach paves the way to the utilization of, among others, plastic PEN/ITO substrate or textile fibers, thus of potential high importance for the integration of anatase TiO_2 into flexible electronics or for smart textiles for instance. We succeeded in obtaining highly desirable porous electrode texture for photonic applications without any means of template, by simply taking advantage of hydrogen evolution to generate mesopores. We also clarify that the crystallization process during thermolysis proceeds in two separated steps, namely dehydration and structural reorganization to form crystalline anatase, the second step being by far the rate limited step. The TiO_2 produced by this method is composed of meso-macro beads assembly whose properties in photovoltaic dye-sensitized solar cell demonstrated one among the best power conversion efficiencies reported so far on flexible dye solar cells, namely a power conversion efficiency of 7.2% under air mass A.M.1.5G standard conditions ($100\ \text{mW}/\text{cm}^2$).

References

- Fujishima, A. & Honda, K. Electrochemical Photolysis of Water at a Semiconductor Electrode. *Nature* **238**, 37–38 (1972).
- Kapilashrami, M., Zhang, Y., Liu, Y.-S., Hagfeldt, A. & Guo, J. Probing the Optical Property and Electronic Structure of TiO₂ Nanomaterials for Renewable Energy Applications. *Chem. Rev.* **114**, 9662–9707 (2014).
- Chen, X., Liu, L., Yu, P. Y. & Mao, S. S. Increasing Solar Absorption for Photocatalysis with Black Hydrogenated Titanium Dioxide Nanocrystals. *Science* **331**, 746–750 (2011).
- Dette, C. *et al.* TiO₂ Anatase with a Bandgap in the Visible Region. *Nano Lett.* **14**, 6533–6538 (2014).
- Zhou, W. *et al.* Ordered Mesoporous Black TiO₂ as Highly Efficient Hydrogen Evolution Photocatalyst. *J. Am. Chem. Soc.* **136**, 9280–9283 (2014).
- O'Regan, B. & Graetzel, M. A low-cost, high-efficiency solar cell based on dye-sensitized colloidal TiO₂ films. *Nature* **353**, 737–740 (1991).
- Graetzel, M. Photoelectrochemical cells. *Nature* **414**, 338–344 (2001).
- Schneider, J. *et al.* Understanding TiO₂ Photocatalysis: Mechanisms and Materials. *Chem. Rev.* **114**, 9919–9986 (2014).
- Bai, Y., Mora-Seró, I., De Angelis, F., Bisquert, J. & Wang, P. Titanium Dioxide Nanomaterials for Photovoltaic Applications. *Chem. Rev.* **114**, 10095–10130 (2014).
- Hagfeldt, A., Boschloo, G., Sun, L., Kloo, L. & Pettersson, H. Dye-Sensitized Solar Cells. *Chem. Rev.* **110**, 6595–6663 (2010).
- Kim, H.-S. *et al.* High Efficiency Solid-State Sensitized Solar Cell-Based on Submicrometer Rutile TiO₂ Nanorod and CH₃NH₃PbI₃ Perovskite Sensitizer. *Nano Lett.* **13**, 2412–2417 (2013).
- Wang, J. T.-W. *et al.* Low-Temperature Processed Electron Collection Layers of Graphene/TiO₂ Nanocomposites in Thin Film Perovskite Solar Cells. *Nano Lett.* **14**, 724–730 (2014).
- Leijtens, T., Lauber, B., Eperon, G. E., Stranks, S. D. & Snaith, H. J. The Importance of Perovskite Pore Filling in Organometal Mixed Halide Sensitized TiO₂-Based Solar Cells. *J. Phys. Chem. Lett.* **5**, 1096–1102 (2014).
- Feng, Q., Wang, T., Zhang, F., Song, B. & Du, K. Synthesis of TiO₂ photocatalytic materials via solid-state reaction and its photodegradation property for methyl orange. *Materials Research Innovations* **18**, S4-92-S94-96 (2014).
- Niederberger, M., Bartl, M. H. & Stucky, G. D. Benzyl Alcohol and Titanium Tetrachloride A Versatile Reaction System for the Nonaqueous and Low-Temperature Preparation of Crystalline and Luminescent Titania Nanoparticles. *Chem. Mater.* **14**, 4364–4370 (2002).
- Wu, M. *et al.* Sol-Hydrothermal Synthesis and Hydrothermally Structural Evolution of Nanocrystal Titanium Dioxide. *Chem. Mater.* **14**, 1974–1980 (2002).
- Pottier, A. *et al.* Size tailoring of TiO₂ anatase nanoparticles in aqueous medium and synthesis of nanocomposites. Characterization by Raman spectroscopy. *J. Mater. Chem.* **13**, 877–882 (2003).
- Deshpande, S. B. *et al.* Room temperature synthesis of mesoporous aggregates of anatase TiO₂ nanoparticles. *Materials Chem. and Phys.* **97**, 207–212 (2006).
- Natarajan, C. & Nogami, G. Cathodic Electrodeposition of Nanocrystalline Titanium Dioxide Thin Films. *J. Electrochem. Soc.* **143**, 1547–1550 (1996).
- Sauvage, F. *et al.* Hierarchical TiO₂ Photoanode for Dye-Sensitized Solar Cells. *Nano Lett.* **10**, 2562–2567 (2010).
- Miyasaka, T. Toward Printable Sensitized Mesoscopic Solar Cells: Light-Harvesting Management with Thin TiO₂ Films. *J. Phys. Chem. Lett.* **2**, 262–269 (2011).
- Kavan, L., O'Regan, B., Kay, A. & Grätzel, M. Preparation of TiO₂ (anatase) films on electrodes by anodic oxidative hydrolysis of TiCl₃. *J. Electroanal. Chem.* **346**, 291–307 (1993).
- Patra, S., Bruyère, S., Taberna, P.-L. & Sauvage, F. Electrodeposition of TiO₂ Using Ionic Liquids. *Electrochem. Lett.* **3**, D16–D18 (2014).
- Patra, S. *et al.* Room-Temperature Synthesis of High Surface Area Anatase TiO₂ Exhibiting a Complete Lithium Insertion Solid Solution. *Part. Part. Syst. Charact.* **30**, 1093–1104 (2013).
- Patra, S., Davoisne, C., Bouanfif, H., Foix, D. & Sauvage, F. Phase stability frustration on ultra-nanosized anatase TiO₂. *Sci. Rep.* **5**, 10928–10937 (2015).
- Izaki, M. & Omi, T. Transparent zinc oxide films prepared by electrochemical reaction. *Appl. Phys. Lett.* **68**, 2439 (1996).
- Halme, J., Saarinen, J. & Lund, P. Spray deposition and compression of TiO₂ nanoparticle films for dye-sensitized solar cells on plastic substrates. *Solar Energy Materials and Solar Cells* **90**, 887–899 (2006).
- Rosca, V., Duca, M., de Groot, M. T. & Koper, M. T. M. Nitrogen Cycle Electrocatalysis. *Chem. Rev.* **109**, 2209–2244 (2009).
- de Voors, A. C. A., van Santen, R. A. & van Veen, J. A. R. Electrocatalytic reduction of NO₃⁻ on palladium/copper electrodes. *J. Molecular Cat. A: Chem.* **154**, 203–215 (2000).
- Nobial, M., Devos, O., Mattos, O. R. & Tribollet, B. The nitrate reduction process: A way for increasing interfacial pH. *J. Electroanal. Chem.* **600**, 87–94 (2007).
- Wheast, R. C. *Handbook of Chemistry and Physics* 63rd edn (CRC press, 1982).
- Aouina, N., Cachet, H., Debiemme-chouvy, C. & Tran, T. T. M. Insight into the electroreduction of nitrate ions at a copper electrode, in neutral solution, after determination of their diffusion coefficient by electrochemical impedance spectroscopy. *Electrochimica Acta* **55**, 7341–7345 (2010).
- Sauerbrey, G. Verwendung von Schwingquarzen zur Wägung dünner Schichten und zur Mikrowägung *Z. Physik* **155**, 206–222 (1959).
- Sugimoto, T., Zhou, X. & Muramatsu, A. Synthesis of Uniform Anatase TiO₂ Nanoparticles by Gel-Sol Method: 1. Solution Chemistry of Ti(OH)_n⁽⁴⁻ⁿ⁾⁺ Complexes. *J. Colloid and Interface Sci.* **252**, 339–346 (2002).
- Elias, J. *et al.* Passing the limit of electrodeposition: 'Gas template' H₂ nanobubbles for growing highly crystalline nanoporous ZnO. *Nano Energy* **1**, 742–750 (2012).
- An, H.-J., Jang, S.-R., Vittal, R., Lee, J. & Kim, K.-J. Cationic surfactant promoted reductive electrodeposition of nanocrystalline anatase TiO₂ for application to dye-sensitized solar cells. *Electrochimica Acta* **50**, 2713–2718 (2005).
- Koelsch, M., Cassaignon, S., Ta Thanh Minh, C., Guillemoles, J. F. & Jolivet, J. P. Electrochemical comparative study of titania (anatase, brookite and rutile) nanoparticles synthesized in aqueous medium. *Thin Solid Films* **451–452**, 86–92 (2004).
- Yang, H. G. *et al.* Solvothermal Synthesis and Photoreactivity of Anatase TiO₂ Nanosheets with Dominant {001} Facets. *J. Am. Chem. Soc.* **131**, 4078–4083 (2009).
- Ma, X. Y. *et al.* Fabrication of uniform anatase TiO₂ particles exposed by {001} facets. *Chem. Comm.* **46**, 6608–6610 (2010).
- Shi, W. *et al.* The synthesis of nitrogen/sulfur co-doped TiO₂ nanocrystals with a high specific surface area and a high percentage of {001} facets and their enhanced visible-light photocatalytic performance. *Nanoscale Res. Lett.* **7**, 1–9 (2012).
- Yang, H. G. *et al.* Anatase TiO₂ single crystals with a large percentage of reactive facets. *Nature* **453**, 638–641 (2008).
- Wang, D. *et al.* Spontaneous Phase and Morphology Transformations of Anodized Titania Nanotubes Induced by Water at Room Temperature. *Nano Lett.* **11**, 3649–3655 (2011).
- Lamberti, A. *et al.* Ultrafast Room-Temperature Crystallization of TiO₂ Nanotubes Exploiting Water-Vapor Treatment. *Sci. Rep.* **5**, 7808 (2015).
- Shastri, A. G., Chae, H. B., Bretz, M. & Schwank, J. Morphology and surface uniformity growth in magnesium oxide dehydration. *J. Phys. Chem.* **89**, 3761–3766 (1985).
- Deb, S. K. Photoconductivity and photoluminescence in amorphous titanium dioxide. *Solid State Commun.* **11**, 713–715 (1972).

46. Tang, H. K. P., Sanjinès, R., Schmid, P. E. & Lévy, F. Electrical and optical properties of TiO₂ anatase thin films *J Appl. Phys.* **75**, 2042 (1994).
47. Chandiran, A. K. *et al.* Doping a TiO₂ Photoanode with Nb⁵⁺ to Enhance Transparency and Charge Collection Efficiency in Dye-Sensitized Solar Cells. *J. Phys. Chem. C* **114**, 15849–15856 (2010).
48. Chandiran, A. K., Sauvage, F., Etgar, L. & Graetzel, M. Ga³⁺ and Y³⁺ Cationic Substitution in Mesoporous TiO₂ Photoanodes for Photovoltaic Applications. *J. Phys. Chem. C* **115**, 9232–9240 (2011).
49. Sauvage, F. *et al.* Dye-Sensitized Solar Cells Employing a Single Film of Mesoporous TiO₂ Beads Achieve Power Conversion Efficiencies Over 10%. *ACS Nano* **4**, 4420–4425 (2010).
50. Chen, Y. *et al.* Effect of Mesoporous TiO₂ Bead Diameter in Working Electrodes on the Efficiency of Dye-Sensitized Solar Cells. *ChemSusChem* **4**, 1498–1503 (2011).
51. Huang, F., Chen, D., Zhang, X. L., Caruso, R. A. & Cheng, Y.-B. Dual-Function Scattering Layer of Submicrometer-Sized Mesoporous TiO₂ Beads for High-Efficiency Dye-Sensitized Solar Cells. *Adv. Funct. Mater.* **20**, 1301–1305 (2010).
52. Chen, D., Huang, F., Cheng, Y.-B. & Caruso, R. A. Mesoporous Anatase TiO₂ Beads with High Surface Areas and Controllable Pore Sizes: A Superior Candidate for High-Performance Dye-Sensitized Solar Cells. *Adv. Mater.* **21**, 2206–2210 (2009).
53. Wang, P. *et al.* Enhance the Performance of Dye-Sensitized Solar Cells by Co-grafting Amphiphilic Sensitizer and Hexadecylmalonic Acid on TiO₂ Nanocrystals. *J. Phys. Chem. B* **107**, 14336–14341 (2003).
54. Yoo, K. *et al.* Completely Transparent Conducting Oxide-Free and Flexible Dye-Sensitized Solar Cells Fabricated on Plastic Substrates. *ACS Nano* **9**, 3760–3771 (2015).
55. Huang, F., Chen, D., Chen, Y., Caruso, R. A. & Cheng, Y.-B. Mesoporous titania beads for flexible dye-sensitized solar cells. *J. Mat. Chem. C* **2**, 1284–1289 (2014).
56. Wang, X., Tang, Q., He, B., Li, R. & Yu, L. 7.35% Efficiency rear-irradiated flexible dye-sensitized solar cells by sealing liquid electrolyte in a groove. *Chem. Commun.* **51**, 491–494 (2015).
57. Fu, N.-Q. *et al.* High-Performance Plastic Platinized Counter Electrode via Photoplatinization Technique for Flexible Dye-Sensitized Solar Cells. *ACS Nano* **6**, 9596–9605 (2012).

Acknowledgements

S.P., C.A., P.L.T. and F.S. wish to acknowledge funding from the Agence National of Research (ANR) under the grant Labex “Store-ex”.

Author Contributions

S.P., C.A., M.T., P.L.T. and F.S. conceived the experiments, carried out data analysis and prepared the manuscript. C.D. performed all T.E.M. investigations. F.S. carried out preparation and characterization of the DSSC devices. All authors discussed the results and commented on the manuscript.

Additional Information

Supplementary information accompanies this paper at <http://www.nature.com/srep>

Competing financial interests: The authors declare no competing financial interests.

How to cite this article: Patra, S. *et al.* Low-temperature electrodeposition approach leading to robust mesoscopic anatase TiO₂ films. *Sci. Rep.* **6**, 21588; doi: 10.1038/srep21588 (2016).



This work is licensed under a Creative Commons Attribution 4.0 International License. The images or other third party material in this article are included in the article’s Creative Commons license, unless indicated otherwise in the credit line; if the material is not included under the Creative Commons license, users will need to obtain permission from the license holder to reproduce the material. To view a copy of this license, visit <http://creativecommons.org/licenses/by/4.0/>